

Article

Short Fiber-Reinforced Polymer Polyamide 6 Lugs and Selective Laser-Melted Ti-6Al-4V Bushing Contact Cohesive Zone Model Mode II Parameters' Evaluation

Andry Sedelnikov ^{1,*}, Evgenii Kurkin ¹, Vitaliy Smelov ², Vladislava Chertykovtseva ¹, Vyacheslav Alekseev ², Andrey Gavrilov ¹, Evgenii Kishov ¹, Maksim Zvyagincev ² and Sergey Chernyakin ¹

- ¹ Institute of Aerospace Engineering, Samara National Research University, 34 Moskovskoe Shosse, Samara 443086, Russia; kurkin.ei@ssau.ru (E.K.); vladislaava.s@yandex.ru (V.C.); gavrilov@ssau.ru (A.G.); evgeniy.kishov@ssau.ru (E.K.); chernyakin.sa@ssau.ru (S.C.)
- ² Institute of Engine and Power Plant Engineering, Samara National Research University, 34 Moskovskoe Shosse, Samara 443086, Russia; smelov@ssau.ru (V.S.); alexeev_v.p@mail.ru (V.A.); zvyagincev.ma@ssau.ru (M.Z.)
- * Correspondence: axe_backdraft@inbox.ru

Abstract: This paper discusses an approach to estimating the parameters of the cohesive zone model (CZM) by mode II by extruding the bushing along the lug axis. This method of evaluation requires small samples, which is particularly relevant when investigating short fiber-reinforced polymers (SFRPs) with additively manufactured embedded elements. Adhesion is investigated on the example of 30% carbon fiber-reinforced polyamide-6 molded to Ti-6Al-4V (VT6) selective laser-melted (SLM) alloy bushing in cases of a roughness $R_a = 2.66 \mu\text{m}$ (vibratory finishing), $R_a = 8.79 \mu\text{m}$ (sandblasting), and $R_a = 10.02$ (directly from SLM). The values of the maximum equivalent tangential contact stress were in a range from 1.1 MPa to 9.5 MPa, while the critical fracture energy for tangential slip was estimated at 15 N/mm for all cases. Experimental validation of the obtained CZM mode II was carried out by evaluating the load-carrying capacity of the lugs with different bushings. In both the experiment and the calculation, greater bushing roughness provides greater lug load-bearing capacity. The ribbed bushings added significant strength in the experiments, which confirmed the importance of considering the tangential mode in the contact model. The presented models can be used for the preliminary evaluation of short fiber-reinforced polyamide-6 parts with titanium-embedded elements bearing capacity.

Keywords: contact; CZM model; SFRP; PA6; Ti-6Al-4V; SLM; strength; roughness; experiment; adhesion



Citation: Sedelnikov, A.; Kurkin, E.; Smelov, V.; Chertykovtseva, V.; Alekseev, V.; Gavrilov, A.; Kishov, E.; Zvyagincev, M.; Chernyakin, S. Short Fiber-Reinforced Polymer Polyamide 6 Lugs and Selective Laser-Melted Ti-6Al-4V Bushing Contact Cohesive Zone Model Mode II Parameters' Evaluation. *Computation* **2024**, *12*, 105. <https://doi.org/10.3390/computation12050105>

Academic Editor: Andrés Amador García-Granada

Received: 6 March 2024

Revised: 3 May 2024

Accepted: 7 May 2024

Published: 17 May 2024



Copyright: © 2024 by the authors. Licensee MDPI, Basel, Switzerland. This article is an open access article distributed under the terms and conditions of the Creative Commons Attribution (CC BY) license (<https://creativecommons.org/licenses/by/4.0/>).

1. Introduction

Composite materials are increasingly being introduced into various industries, including the aerospace industry [1,2].

The strength of pin-joints has a great influence on the strength of the product. Lugs are an important element in aerospace designs because they connect wings to the fuselage, engines to pylons, flaps, ailerons, and spoilers to wings [3]. During operation, the lugs are subjected to cyclic loads [4,5]. High stress concentrations can lead to cracks and their subsequent growth under loading [5,6]. It is important to develop damage-resistant design criteria and analysis methods to ensure the high performance and reliability of aircraft lug attachments [7,8].

To transfer local reinforcement in products made of composite materials, it is necessary to use embedded elements or bushings in places where concentrated loads are applied [9,10]. Currently, the design and production of embedded elements is based on the use of simple standard shapes manufactured by mechanical processing [11]. Such embedded elements are characterized by excess weight, which has a particularly negative impact on the weight efficiency of aerospace products consisting of many parts. The use

of topology optimization methods implies working with one material in the design area and does not allow considering the stiffness of the material surrounding the load-bearing design elements [12–14]. Injection molding methods [15] and additive technologies [16] are often used to produce topologically complex designs. Low adhesion of embedded elements to the base material has a significant impact on the stress-strain state of the design and leads to a multiple reduction in its load-bearing capacity [17].

About 50% of titanium used in the aerospace industry is Ti-6Al-4V alloy, which has a good combination of performance and technological properties [18,19]. The high strength of Ti-6Al-4V alloy is achieved through heat treatment [20]. Compared with commercial pure titanium, Ti-6Al-4V alloy is more suitable for large-scale industrial applications, such as titanium hybrid bonding [21]. According to test data [22], the tensile strength of the Ti-6Al-4V alloy produced using selective laser melting (SLM) technology is slightly inferior to the tensile strength of the alloy obtained by rolling and stamping [23], which indicates the high performance properties of the material. One of the main goals of the aerospace industry is to create lightweight designs. One approach is to use different materials, resulting in dissimilar bonds, such as metals and fiber-reinforced composites [24]. The following technologies are used for titanium/polyamide bonding: induction technologies [25]; adhesion; hot-pressing technology [26]; mechanical assembly (such as riveting, screwing, or snap jointing); or welding [27,28]. Surface preparation is the most important step in the process and influences the quality of the adhesive bond [29]. Various methods have been used to increase the adhesive strength between the connecting part and the embedded element [30–33]. A method for treating metal surfaces to enhance adhesion is chemical treatment [29,34]. The authors [35] showed that the thickness of the oxide layer significantly influences the mechanical characteristics of the bond. The titanium/polyamide bond with a thick oxide layer showed lower load capacity, and with UV irradiation, a more pronounced decrease in bond strength was observed. Experimental studies [36] revealed that surface cleaning, surface modification, and sodium hydroxide anodization of titanium resulted in significantly high peel strengths for a titanium/aluminum bond. Recent testing of adhesive bonds has shown that pre-treating the metal surface with a laser can also significantly increase the strength of the entire pin-joint [36–38]. The modern method for producing hybrid bonds is injection molding, which combines automation, process speed, cost-effectiveness, and dimensional accuracy [39]. The mechanical properties of a bond are also affected by the manufacturing process: in-mold assembly and post-mold assembly [40]. A method for bonding titanium to the molding polymer designs is described in [41].

Advances in additive manufacturing have enabled the use of reliable industrial lasers, high-performance software, cost-effective equipment, and advanced raw materials for aerospace manufacturing [42]. Selective laser-melted parts can achieve full compaction with minimal defects if process parameters are carefully optimized [43,44]. Thus, process parameters must be correctly selected for each new material system [45]. Article [46] reviews the critical aspects of optimizing processing parameters affecting the properties of selective laser-manufactured titanium alloys and titanium matrix composites and critically evaluates the future prospects of such materials.

The cohesive zone material (CZM) model [47], depending on the normal component (mode I) and the tangential component (mode II), is usually used to describe the mechanics of adhesive interaction. A comparative modes analysis is presented in [48]. Delaminations can grow rapidly under mode I or mode II interlaminar fatigue loads [49–51], which significantly limits the acceptable damage size for aircraft composite designs. In some cases, a mixed mode model is used, which considers both directions of destruction [52]. It was noted in [53,54] that materials demonstrate higher resistance to mode II crack propagation compared to mode I. The work [55] shows the effectiveness of increasing the roughness of the bushing and using stiffeners to reduce the mass of the bond. It was noted that mode II has the greatest impact on reducing the mass of the entire lug. Coefficients of the CZM model for composite/metal bonds are defined in [26,56–59]. The work [60] also notes a higher critical strain energy release rate for mode II compared to mode I. Moreover, mode I is difficult to measure and requires

long samples [61]. The parameters of the contact interaction between metals and polymers are presented in [39]. Among the forty studies presented, contact interaction with titanium is presented only in one work [41] using the example of assessing the interaction of the PPS30GF/Ti6Al4V bond; therefore, assessing the parameters of the contact of carbon filled polyamide 6 (PA6) with titanium alloys is relevant.

The goals of this study are to evaluate the parameters of the contact interaction model between parts made of thermoplastic short-reinforced composite materials based on polyamide-6 and embedded elements with different surface roughness values, made of titanium alloys manufactured by selective laser melting; and to evaluate the influence of the roughness of titanium-embedded elements on the load-bearing capacity of designs. The study of the adhesive interaction model was carried out using lugs as an example because they are often encountered in practice, are easy to manufacture, and allow, through various loading methods, to obtain the characteristics of the contact model and verify this model. Ring-shaped bushings are produced by the SLM method for experimental purposes, but the use of the SLM method for the production of bushings of more complex shapes obtained also by topological optimization, opens the way for a significant increase in short fiber-reinforced polymer (SFRP) structures' load capability. The novelty of the work is the use of axial bushing extrusion to determine the parameters of adhesive interaction between the plastic part and the embedded element. This makes it possible to significantly simplify the estimation of contact parameters in cases where the fabrication of large crack opening specimens is difficult due to process limitations, such as shrinkage or limitation of SLM capabilities.

2. Materials and Methods

2.1. Materials and Material Models

The material chosen for the lug is polyamide-6, reinforced with 30% short carbon fibers—a structural material with high weight efficiency and the technological ability to be molded using thermoplastic machines at temperatures from 220 to 270 °C. The study of the characteristics of the short-reinforced polyamide used for the manufacture of the lugs is presented in detail in [62] and includes the determination of the parameters of anisotropic models of the material used in the current work for numerical modeling. VT6 (Ti-6Al-4V) titanium, widely used for the SLM process and capable of withstanding high contact stresses, was chosen as the material for the embedded elements. A detailed study of the characteristics of the VT6 alloy used is presented in [21].

Tensile tests were performed on five samples of 1BA-type according to the ISO 527-2 [63] standard of polyamide-6 reinforced with 30% of the mass with short carbon fibers (UPA 6 30 M, Gamma-plast, Moscow, Russia [64]) on a universal testing machine Zwick/Roell Z050 TE, ZwickRoell, Singapore [65] (see Figure 1). The compliance of the material model used in the strength calculations [62] with the mechanical characteristics of the samples in molding direction was confirmed.

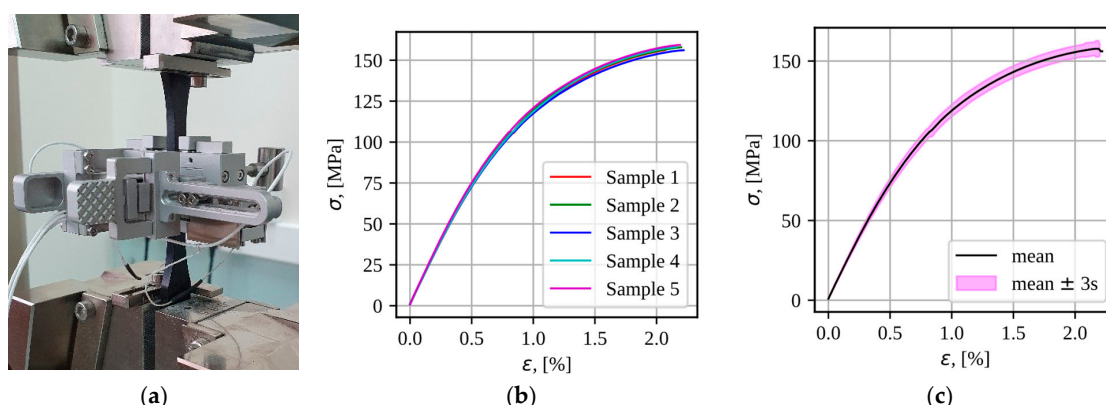


Figure 1. Tensile test samples PA6 + 30% carbon fibers ISO 527-2 type 1BA: (a) test; (b) tensile curves; (c) mean value \pm 3 corrected sample standard deviation.

2.2. Methods

2.2.1. Problem Statement and Lugs Geometry

The study of the adhesion interaction model was conducted using lugs as an example (see Figure 2). A previous study of the sensitivity of lug sizes to the characteristics of contact interaction [55] showed that the maximum permissible stress in mode II of failure in the contact between the lug and the bushing has the greatest influence on the optimal lug bridge size. We will determine the dimensions of the lugs based on the experience gained in [55] in optimizing the sizes of lugs depending on the characteristics of the contact interaction. The diameter of the lug axis is 12 mm, the lug length from the axis to the embedment is 56 mm, the size of the lugs for embedding in the experimental study is 12 mm, and the thickness of the lugs is 5 mm. The lug width is determined by the size of bridge b . Assuming the transmission of force at a level of 5000 N, we will choose lugs of two standard types S and M, differing in the width of the bridge b : for the S-type, b is 5 mm, for the M-type, b is 10 mm. S-type lugs rely more on load transfer through adhesion between the bushing and the lug, whereas M-type lugs rely more on bridging the plastic component of the part. The thickness of the bushing for such a lug, based on the strength limits of titanium and the manufacturability of production, is 1 mm.

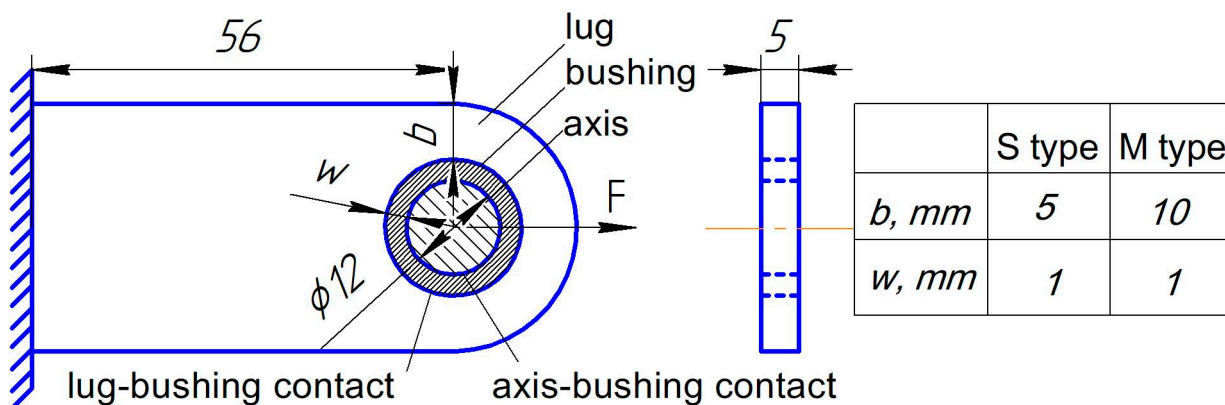


Figure 2. Statement of the problem.

In addition, the paper presents two kinds of lugs for comparison: lugs without a bushing manufactured in the same molds S- and M-types and lugs with a ribbed bushing. The lugs without bushings have a 1 mm wider bridge due to the bushing elimination. Bushings with ribbing consist of 50 ribs with a wave length of 0.87 mm and wave depth of 0.3 mm (thickness is in diapason from 0.7 mm to 1 mm).

2.2.2. CZM Model

The adhesive layer was considered by using contact elements in Ansys Mechanical APDL. The bilinear CZM model was used [66]. Since mode II has the greatest impact on reducing the mass of the entire lug [62], we chose a model based on mode II as the basis for predicting the load-bearing capacity of the lugs.

When describing the contact interaction tangential stress was considered [66]:

$$\sigma_t = k_t u_t (1 - d_t), \quad (1)$$

where σ_t —tangential contact stresses, MPa; k_t —tangential contact stiffness, N/mm³; u_t —tangential slip distance, mm; $u_t = \sqrt{u_1^2 + u_2^2}$, u_1 , and u_2 —slip distances in the two principal directions in the tangent plane, and d_t —debonding parameter. In the presence of compressive forces, the CZM model prevents penetration of the contacting surfaces. In the case of unloading and subsequent reloading, the CZM model considers the debonding parameter [19], which is defined as follows:

$$d_t = \left(\frac{u_t - \bar{u}_t}{u_t} \right) \left(\frac{u_t^c}{u_t^c - \bar{u}_t} \right), \quad (2)$$

for $\Delta_t > 1$ and $d_t = 0$ for $\Delta_t \leq 1$ where, $\Delta_t = u_t / \bar{u}_t$, \bar{u}_t —tangential slip distance at the maximum tangential contact stress, mm.

The tangential critical value u_t^c is calculated based on the critical energy release rate G_t and maximum critical stress σ_t^c , which are parameters of the contact model [66]:

$$u_t^c = \frac{2G_t^c}{\sigma_t^c}. \quad (3)$$

The process of convergence of the Newton–Raphson algorithm at a nonlinearity of the debonding type can be challenging; therefore, artificial damping was used to accelerate and stabilize the convergence process, which limits the amplitude of the change in the destruction parameter during the transition from one iteration to another:

$$d_v = \frac{d\Delta t + d_{old}\eta}{\Delta t + \eta}, \quad (4)$$

where Δt —the time step (in the case of a static calculation, the time varies from 0 to 1 and is fictitious, simply determining the current load value), d_{old} —the destruction parameter in the previous step, and η —the damping coefficient. The damping coefficient must be small compared to the time step to avoid introducing significant errors into the calculation. In this study, the damping coefficient was set to 0.01.

The values that determine the properties of the contact interaction of the bushing and the lug body were σ_t^c, G_t^c, η .

2.2.3. Determination of Contact Properties

The parameters of adhesive interaction in mode II, which determines the fracture caused by shear, corresponds to the case of bushing extrusion along the lug axis. The characteristics of mode II fracture along the tangential direction correspond to shear loading, which manifests when the bushing is extruded along the axis of the lug. This approach has advantages compared to using specimens according to the standard test method [67]: samples for the identification of adhesion parameters are in conditions closer to the lug under study than standard [67] samples; the proposed samples are much smaller in comparison with [67] samples, which is especially important in the SLM Ti-6Al-4V production case, and testing samples can be made in an existing mold. The tool for bushing extrusion along the axis consists of a base and peen (Figure 3) and is intended for use in conjunction with sample compression grips on a universal testing machine Zwick/Roell Z050 TE [65]. The base was made from the D16T aluminum alloy [10,68], similar to the 2024-T4 aluminum alloy [69]. The peen was made from structural steel. The diameter of the top of the peen is 13 mm, allowing overlap of half the bushing thickness, while the base hole diameter is 15 mm, which is 1 mm larger than the external bushing diameter. The bushings were made to fit G8 with an overlap nominal diameter at 0.03 mm. The peen and base were manufactured after the bushings, considering their nominal diameter, with a g8 peen fit (reduced nominal diameter at 0.03 mm) and a G8 base fit (overlap nominal diameter at 0.03 mm). Such tolerances give a sliding fit with a 0.06 mm gap between the peen and bushing and between the peen and base. This provides, on the one hand, coaxially between the base and bushing and, on the other hand, reduces the influence of friction on the experimental results. The tool design allows us to organize the shear loading during bushing extrusion and investigate the dependence of CMZ mode II fracture model parameters from the roughness of embedded elements.

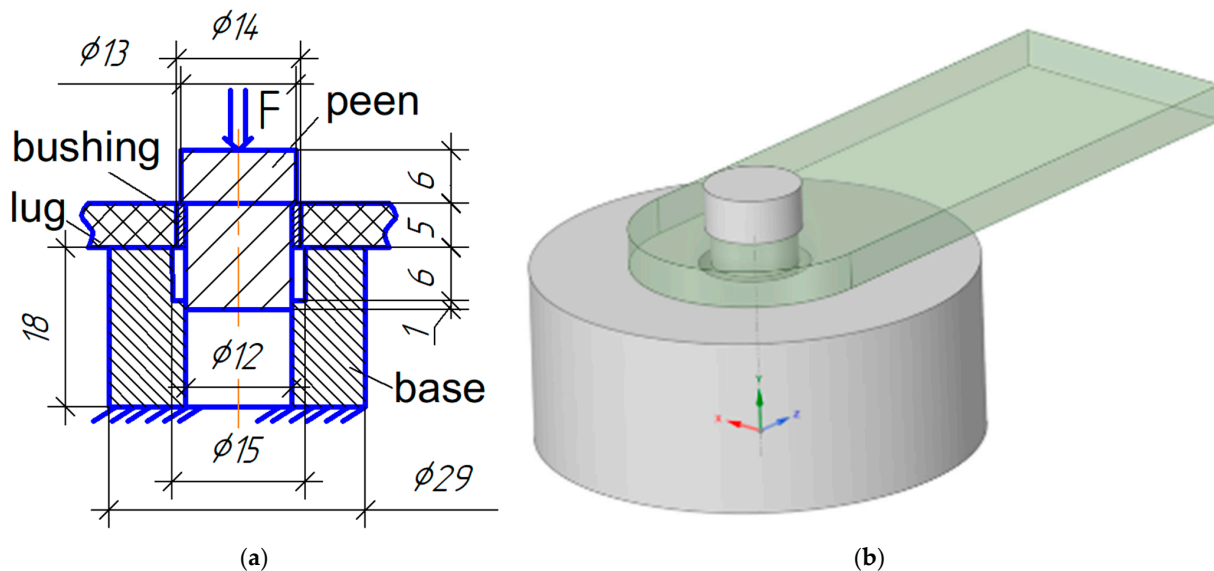


Figure 3. Test scheme for determining the characteristics of the adhesion interaction model in mode II (tangential), (a) scheme of load, (b) 3d model of tool.

2.2.4. Determination of the Load-Bearing Capacity of Lugs with Bushings

The load-bearing capacity of lugs with various embedded elements was assessed by tensile tests on a servo-hydraulic machine, Shimadzu EHF-E [70].

A tool for the tensile testing of lugs has been manufactured (see Figure 4). The tool allows you to measure both the movements of the entire lug and separately control the displacement of the rear wall of the lug axis by installing an extensometer. A sliding fit g8/G8 is also used between the axle bolt and the bushing.

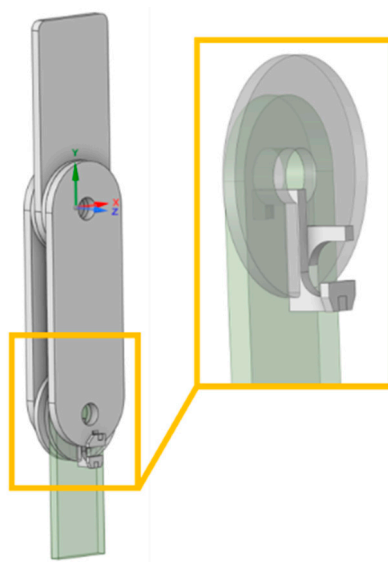


Figure 4. Test scheme for determining the load-bearing capacity of lugs.

2.2.5. Manufacturing of Embedded Elements

The production of titanium-embedded mold elements was carried out using an additive installation 3DLAM Mid. The cost of manufacturing a bushing using the SLM method from titanium alloy powder VT6 is USD 5. The labor intensity of manufacturing 42 pieces is 3 h.

The 3DLAM Mid selective laser melting system is designed for single and small-scale production of arbitrary-shaped parts by layer-by-layer selective fusion of metal powders

with grain size 50 μm . Process parameters were controlled using the software 3DLAM Slicer 2.11. The technological parameters of the SLM were selected experimentally and are shown in Table 1. After assigning the main technological parameters of the selective laser melting (SLM) process, a work file for manufacturing the part was generated. The manufacturing process is shown in Figure 5.

Table 1. Technological parameters of the SLM process.

Parameter	Value
Laser power, W	240
Scanning speed, mm/s	800
Scanning step, mm	0.09
Layer thickness, μm	50

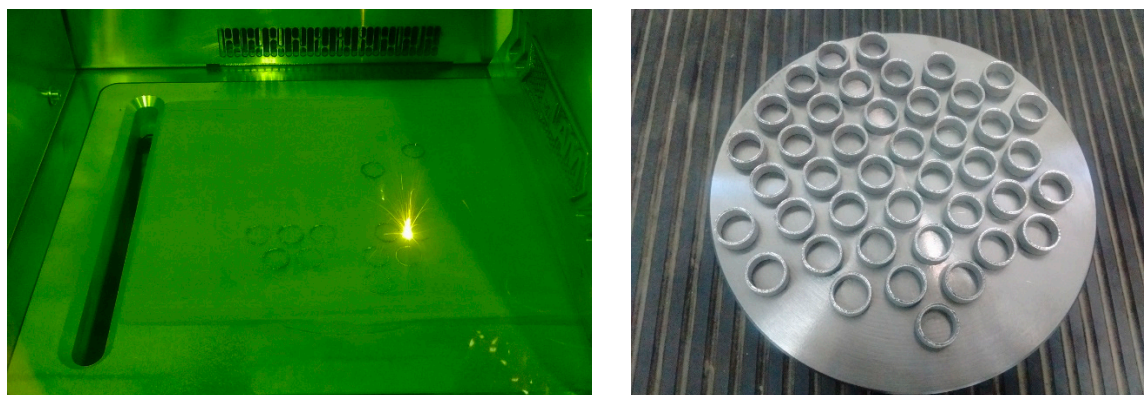


Figure 5. Manufacturing process of embedded elements.

Separation of the workpieces from the construction platform was performed using electrical discharge machining. After separation from the construction platform, mechanical processing of the samples was performed to bring the landing dimensions to the accuracy required for the molding process. Providing gaps between the mold and the embedded element in the range of 0.05–0.1 mm allowed for the easy removal of molding parts but did not allow plastic to penetrate the gaps between the embedded elements and the mold.

The embedded elements are divided into three groups according to the degree of roughness—the first part of the elements is left with the roughness obtained in the SLM process, the second part is subjected to sandblasting, and the third part is vibratory finishing (see Figure 6).



Figure 6. The roughness: (a) sandblasting, (b) vibratory finishing.

Because the results of the parametric study revealed a high role of the shear strength of the contact, it was selected to additionally manufacture bushings with ribs. More than 50 embedded bushings were manufactured—from 5 to 7 of each roughness (vibratory finishing, sandblasting, initial SLM process, ribs) for each of the two standard types of the lug and more than 40 flat samples of two types of embedded elements (14 flat samples for each degree of roughness).

2.2.6. Measuring the Roughness of Samples

After surface treatment, the roughness of flat samples was studied using a profilometer (see Figure 7).



Figure 7. Roughness measurement.

2.2.7. Manufacturing of Samples of Lugs

The lug molding tool was made of steel by milling on a computer numerically controlled (CNC) machine. The heating of the tool was performed using air heating elements. Tool cooling is not required because of the small series and long molding cycles. Injection molding of designs with embedded elements and samples made of short-reinforced composite material was performed on a Negri Bosi VE1700-210, Negri Bosi, Rugby, UK electric injection molding machine [71] (see Figure 8). A preliminary simulation of the injection molding process was performed using Moldflow. The selected gate location causes the weld line to be in the lug area. However, on the one hand, the weld line is not located on the side of the lug hole, which is the most loaded location. On the other hand, in cases of structures with several lugs, molding of some lugs occurs from the part side, and the considered weld line location is typical. In addition, to eliminate the weld line on the front of the lug, a gate would have to be located there, which would necessitate machining the front of the lug and could introduce additional errors into the experiment being conducted.



Figure 8. Injection molding process.

3. Results

3.1. Manufacturing of Samples of Embedded Elements and Lugs

To prepare embedded elements for 3D printing, finite element modeling of the SLM process was performed using the Simufact Additive 21 CAE system (Figures 9 and 10). The boundary conditions correspond to the values of the technological parameters: 240 W laser power, 800 mm/s scanning speed, 90 μm scanning step, and 50 μm layer thickness. The physical properties of titanium were loaded from the built-in database of the CAE system. The degrees of freedom are limited by the lower contact surface of the samples with the build plate. Based on the technological parameters, the inherited deformations of the single-name calculation method are equal to $\epsilon_x = -0.0069$, $\epsilon_y = -0.0045$, and $\epsilon_z = -0.03$. The size of the equilateral voxel finite elements was 0.5 mm, and the calculation results were projected onto the surface mesh of the 3D model of the samples after calculation. The equivalent stress does not exceed the limit of 1200 MPa. Deviations in the shape of samples after the SLM process are -0.05 to 0.25 mm (Figure 10).

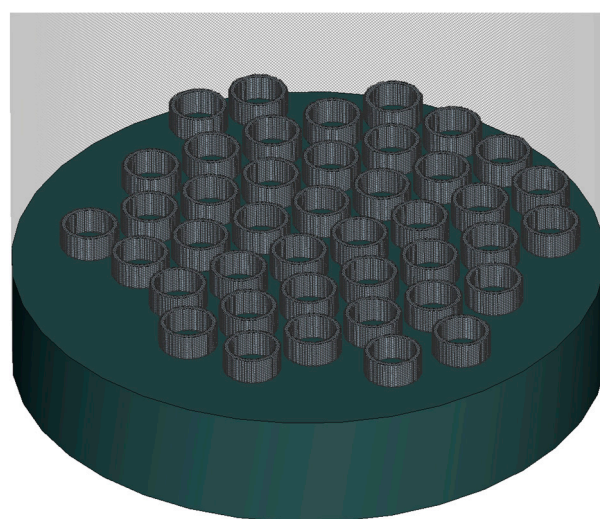


Figure 9. Computational mesh for Simufact Additive analysis.

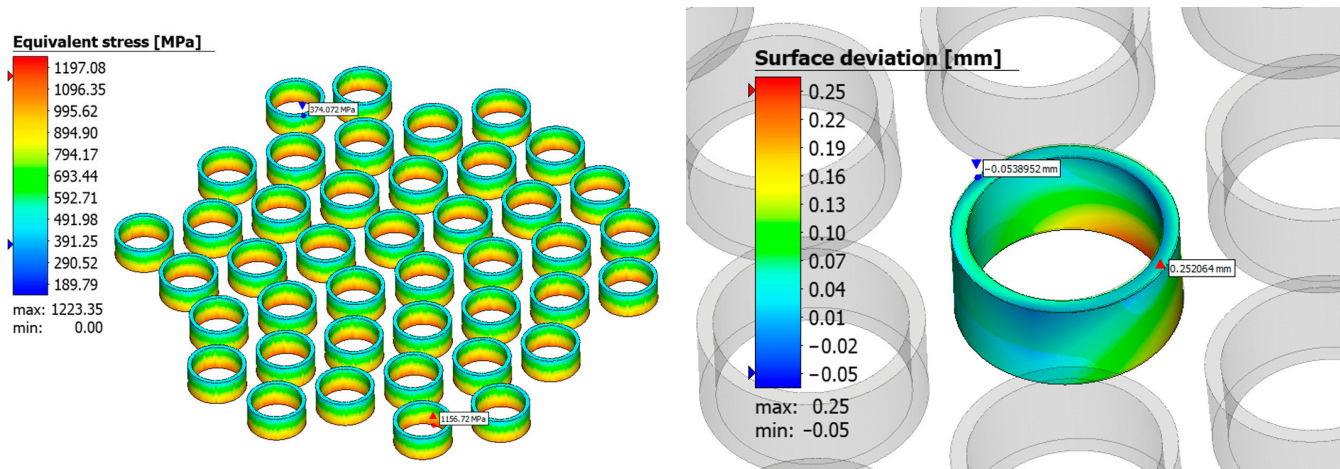


Figure 10. Equivalent stress and surface deviation at SLM process.

The production of titanium-embedded elements was carried out using a 3DLAM Mid additive machine. Process parameters are controlled using the 3DLAM Slicer software. More than 50 embedded bushings and more than 40 flat samples of three roughnesses were manufactured using the SLM method. The three types of roughness are provided by the SLM process, sandblasting, and vibratory finishing (Figure 11).

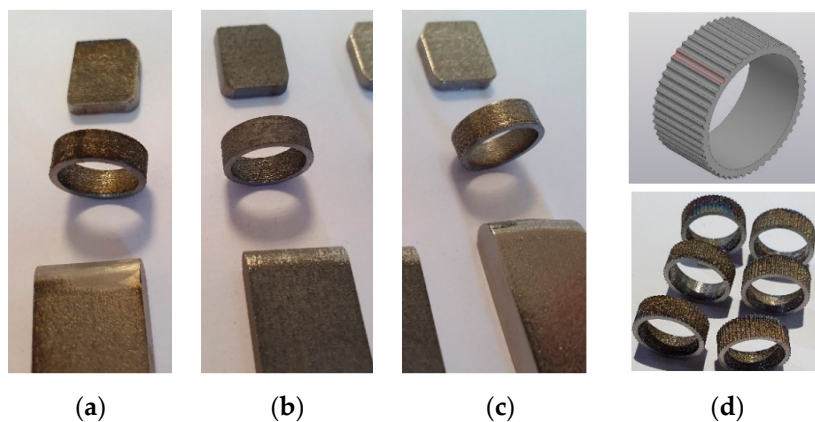


Figure 11. The roughness: (a) SLM process; (b) sandblasting; (c) vibratory finishing; (d) ribbing.

Measurements of the surface roughness of samples of each type showed that the used additive technology produces a surface with a roughness of $R_a = 10 \mu\text{m}$, sandblasting reduces the roughness to $8.8 \mu\text{m}$, and vibratory finishing provides a surface with a roughness of $2.7 \mu\text{m}$ (Table 2).

Table 2. Measurement results.

Surface	$R_a, \mu\text{m}$	CV, %
Vibratory finishing	2.66	24.6
Sandblasting	8.79	24.9
SLM	10.02	17.9

More than 35 molded parts were made, each of which contained lugs of two standard types and samples (Figure 12).



Figure 12. Manufactured lugs.

3.2. Experimental Determination of Mechanical Characteristics of Contact

A tool was designed and manufactured that allows extruding the lug bushing using clamps to compress the samples (Figure 3) on a universal testing machine, Zwick/Roell Z050 TE [65]. Ten lugs of M type were tested for extrusion, three samples each with bushings after vibratory finishing and sandblasting, and four samples with the original surface after the SLM process (Figures 13 and 14).

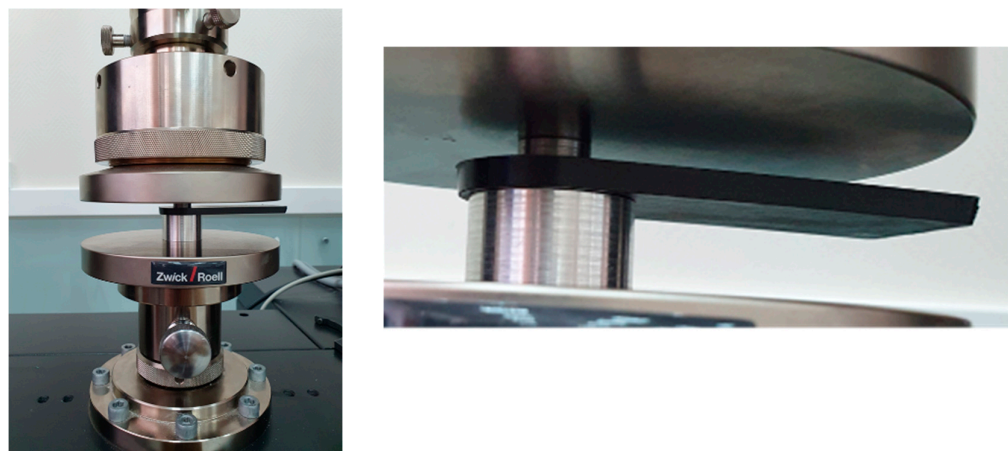


Figure 13. Tests for extrusion of the bushing along the axis.

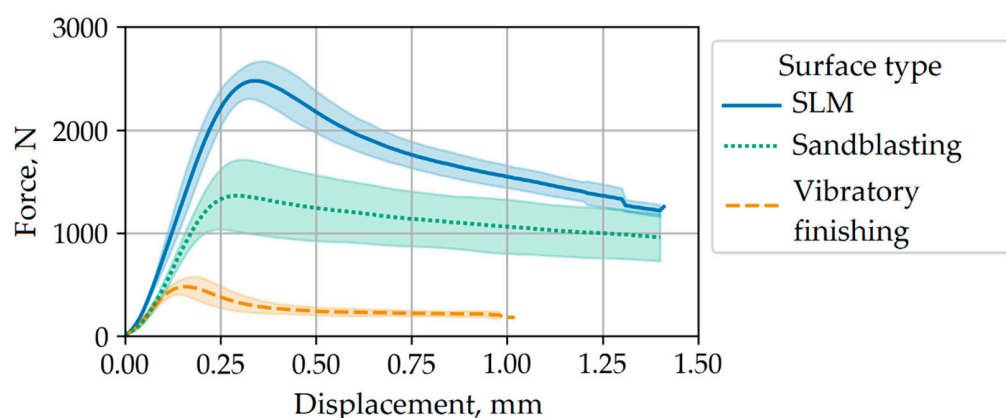


Figure 14. Experimentally obtained force from displacement for extrusion of the bushing along the axis with different embedded elements and surface types. The shadows correspond to \pm one standard deviation.

The parameters of the adhesion interaction model for mode II were fitted on the basis of studies on the extrusion of bushings along the axis. To achieve this, the finite element problem of extruding the bushing from the lug along its axis is solved. The mesh consists of 1614 second-order solid elements with an element size of 0.7 mm inside a 12 mm radius sphere with the origin at the middle of the lug axis (Figure 15a). The solution was conducted for isotropic materials with $E_0 = 7$ GPa and $\nu_0 = 0.35$ for the plastic part and $E_1 = 96$ GPa and $\nu_1 = 0.36$ for the bushing. The bottom surface of the lug is constrained with deformable behavior remote displacement along all axes and rotations inside the pinball region with a 15 mm radius. The upper surface of the bushing is loaded by displacement ($-0.025, -0.05, -0.1, -0.2, -0.3, -0.4$ mm) in the Z direction. The CZM mode II contact describes the connection between the lug and the bushing (Figure 15b). The maximum equivalent tangential contact stress and the rate of energy release were selected based on the experimental data (Figure 14), and the artificial damping coefficient was 0.03 s for all cases. Calculation was performed in ANSYS Workbench 2022R1 on an Intel Core i7-7700K CPU. The total CPU time for the main thread was 101 s, and the total CPU time summed for all threads was 348 s (convergence shown at Figure 16).

The dependence of the force reaction at the bushing displacement boundary condition on the displacement value was fitted to Figure 14 by varying the maximum equivalent tangential contact stress and the rate of energy release to peak force values and force values in the slip presence best match (Figure 17). The overestimated rigidity of the solution before contact failure is associated with the rigidity of the fastening in the test equipment and does not have a decisive effect on the strength characteristics of the CZM model contact

parameters. It is shown that vibratory finishing corresponds to a maximum equivalent tangential contact stress of 1.1 MPa, sandblasting corresponds to 5 MPa, and the original SLM technology provides a contact shear strength of 9.5 MPa. The rate of energy release in this case is 15 kJ m^{-2} .

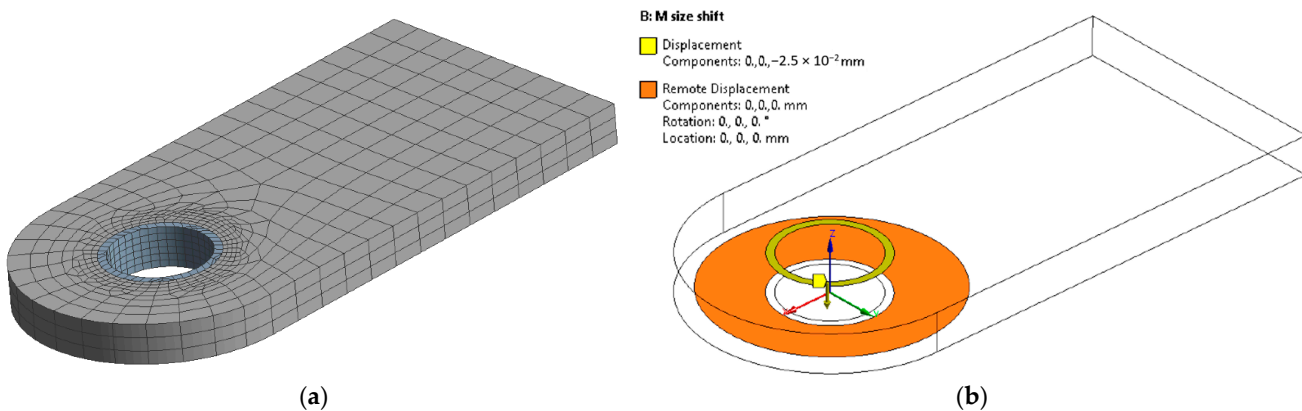


Figure 15. CZM model II parameter identification problem: (a) computational mesh; (b) boundary conditions.

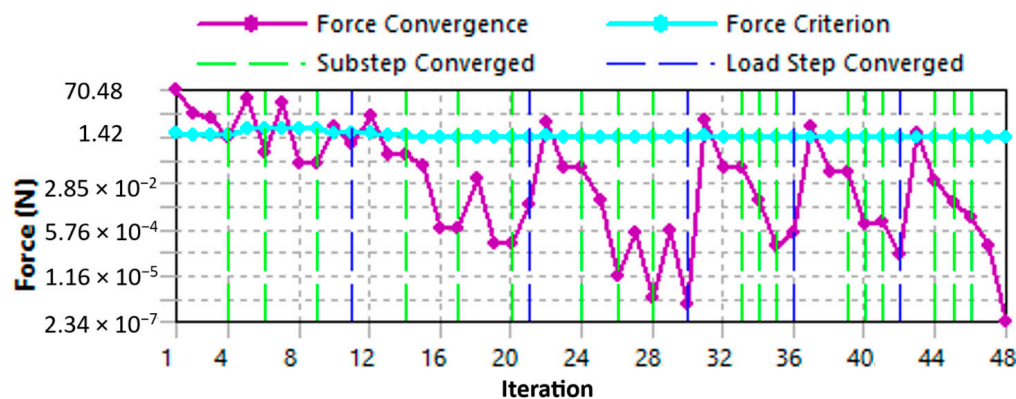


Figure 16. Bushing extruding along lug axis calculation convergence plot.

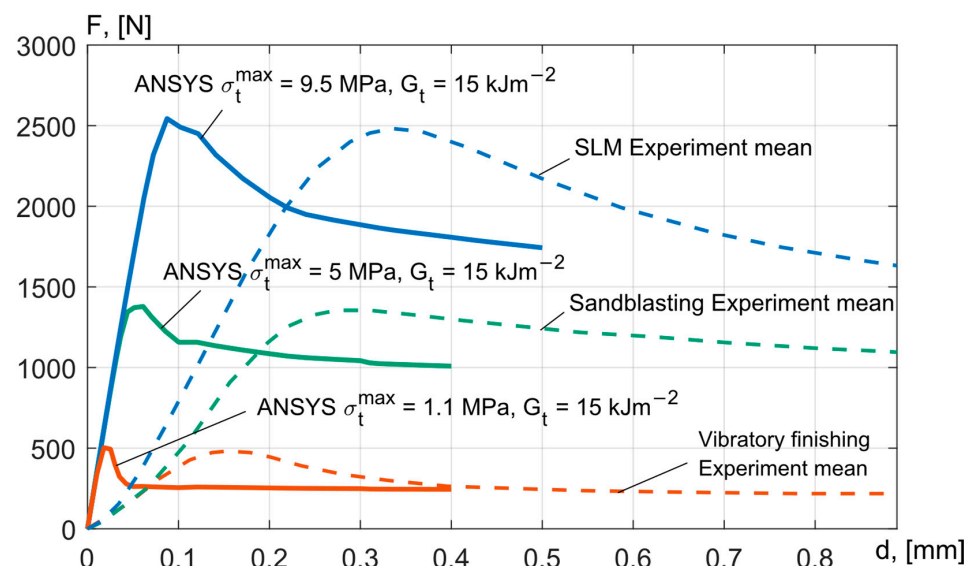


Figure 17. Calculation of extrusion of the bushing along the axis of the lug with different parameters of CZM mode II model.

3.3. Molding Analysis and Validation

A comparison was made of the strength and rigidity of designs with embedded elements made of short-reinforced composite materials, obtained experimentally (partially filled) and by calculation, considering the anisotropy of the material model. To consider the anisotropy of the lug, a thermoplastic molding calculation was performed using the Autodesk Moldflow 2021.1 system, including the calculation of the orientation of the reinforcing fibers. The computational mesh consists of 766,931 elements of tetragonal shape; the average element size is 1.13 mm (Figure 18).

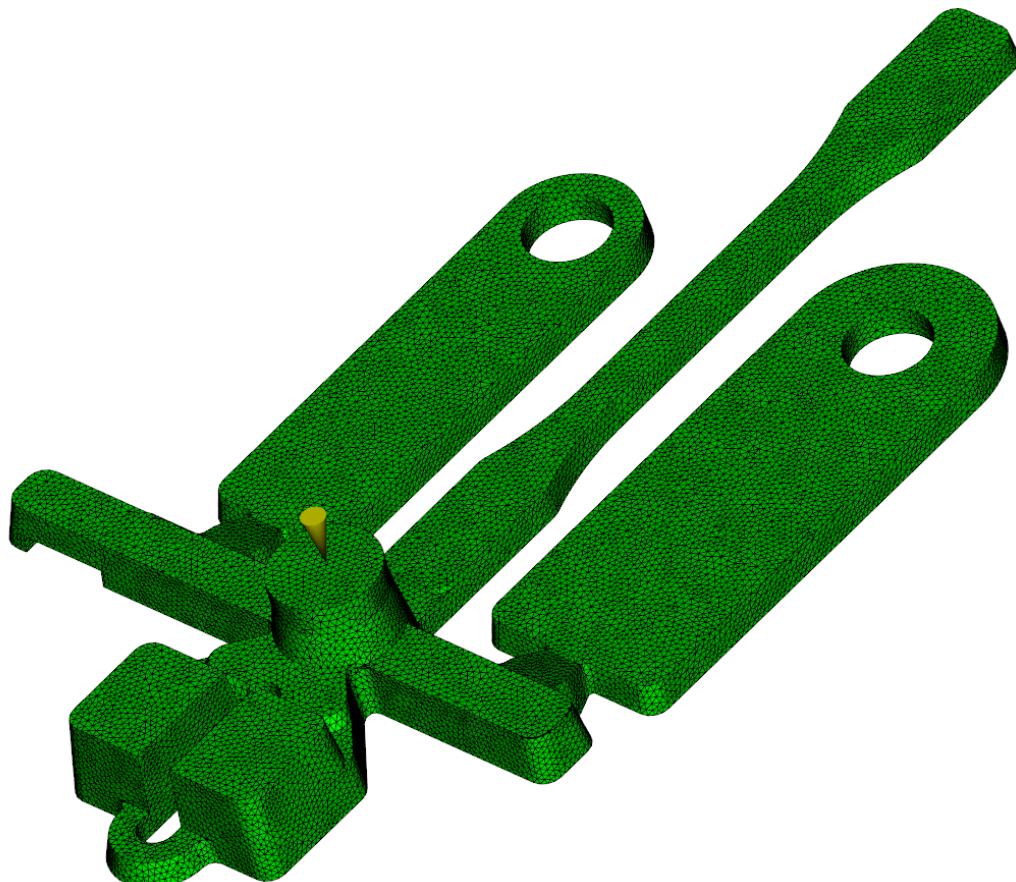


Figure 18. Computational mesh for molding of lugs. Green is cavity, yellow is sprue location.

The rheological characteristics of polyamide-6 reinforced with 30% carbon fibers correspond to the characteristics of Akromid B3 ICF 30 black (5119) (Akro-Plastic GmbH [72]), the viscosity of which is described by the Cros-WLF model [73] with the following parameters:

$$\eta = \frac{\eta_0}{1 + \left(\frac{\eta_0 \dot{\gamma}}{\tau^*}\right)^{(1-n)}}; \quad (5)$$

$$\eta_0 = D_1 \exp\left[\frac{-A_1(T - T^*)}{A_2 + (T - T^*)}\right] \quad (6)$$

where η_0 —temperature-dependent zero shear viscosity; $\tau^* = 193.312$ Pa; $n = 0.3$; $T^* = D_2 + D_3 p$; $D_1 = 1.18e \cdot 10^{23}$; $D_2 = 324.99$ K; $D_3 = 0$; $A_1 = 58.255$; $A_2 = 51.6$ K—constants obtained experimentally. The mold temperature was 85 °C, melt temperature 230 °C, flow rate 15 cm³/c, velocity/pressure switch-over by injection pressure = 40 MPa, and cavity volume is 56 cm³. The calculation was performed on a computer with Win 10, Intel Core i7-7700K, and the CPU time was 6110 s and wall clock time was 1625 s. Figure 19 shows the fill time, the first eigenvalue and first eigenvectors of the fiber orientation tensor, and the weld lines'

position. The calculated fiber orientation tensor is used later for static structural analysis considering the composite material anisotropy.

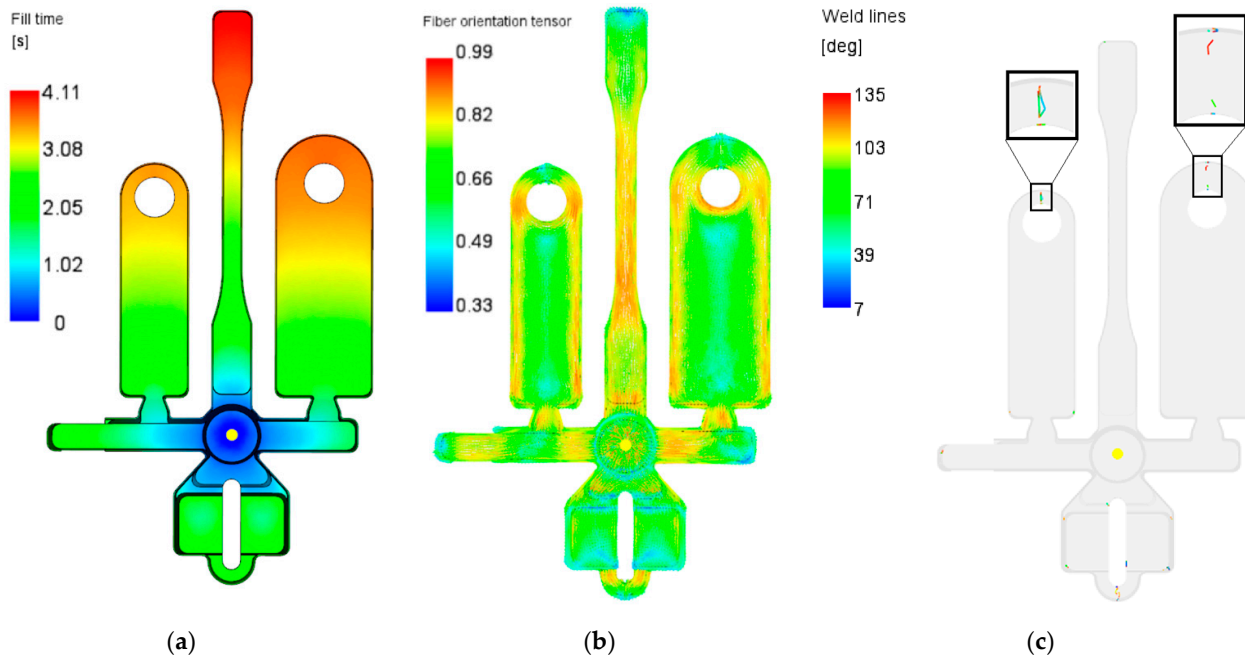


Figure 19. Simulation results of lug molding: (a) fill time; (b) first eigenvalue and first eigenvectors of fiber orientation tensor; (c) weld lines.

The calculation was verified by determining the correspondence between the calculated (colored) and experimentally observed (black) molding fronts (see Figure 20). The validation of the fiber orientation tensor calculation for 30% carbon fibers PA6 using Moldflow can be found in [10].

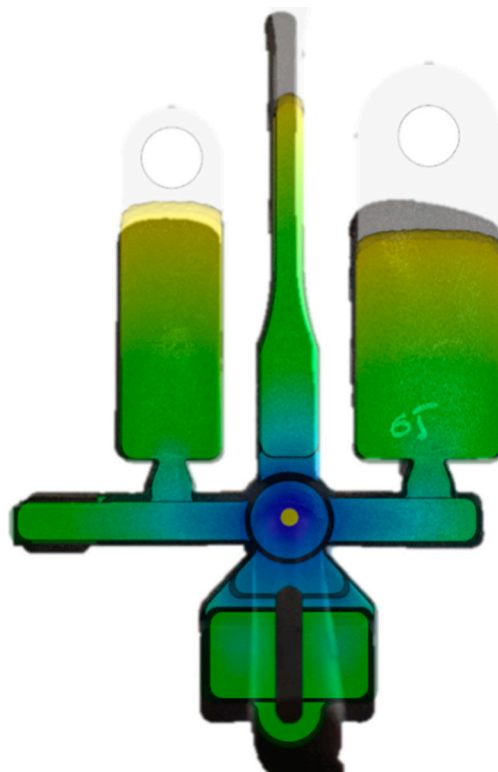


Figure 20. Comparison of calculated and experimentally obtained molding fronts.

3.4. Experimental Determination of the Load-Bearing Capacity of Lugs with Bushings

Sixty samples of lugs were tested—two standard types, S and M, with five surface options for embedded elements (vibratory finishing; sandblasting; SLM, bushing with ribs, with the original roughness of SLM process; lugs without bushing) (see Figure 21, Table 3). A lug without bushings has the same external contours and axis diameter. Therefore, the elimination of the 1 mm thick bushing results in an increase in the bridging width from 5 mm to 6 mm that leads to a higher load-bearing capacity than that of lugs with vibratory finishing bushings with low adhesion.



Figure 21. Test to determine the load-bearing capacity of lugs.

Table 3. Load-bearing capacity of lugs with different surfaces of embedded elements.

Surface	F max, N	CV, %	F max, N	CV, %
	S-Type		M-Type	
Vibratory finishing	4886	6.96	7457	6.54
Sandblasting	5186	3.39	7302	5.10
SLM	5429	1.63	7722	1.73
Ribbing	6029	1.24	8388	2.48
Without bushing	5008	1.72	7551	6.71

3.5. Verification of the Contact Interaction Model

We consider the orientation of the reinforcing fibers that makes it possible to use the anisotropic Tsai–Hill strength criterion [74,75] in the 3D transversely isotropic formulation, which allows one to correctly predict the strength of short-reinforced composite materials since the field of equivalent von Mises stresses cannot correctly consider the anisotropic behavior of plastics, for example, destruction in the lug nose of size S caused by the presence of a weld line. The Digimat material model parameters correspond to the exponential and linear hardening law for 30% carbon fibers' mass fraction [62] and are $E_0 = 3994$ MPa, $\nu_0 = 0.372$, $\sigma_Y = 14.5$ MPa, $k = 188.4$ MPa, $m = 458.3$, $R_\infty = 37.0$ MPa, and fiber AR = 16.54. Composite stress limits in local axes are axial tensile strength = 153 MPa, in-plane tensile strength = 98 MPa, and transverse shear strength = 84 MPa.

The calculation was carried out in ANSYS Workbench 18.2. The computational mesh consisted of 14,175 first order elements for the S-type lug and 37,464 elements for the

M-type lug. The axle element size is 1.5 mm, bushing is 1.0 mm, the lug element size is not uniform and is adjustable. The Sphere of Influence is 1.0 mm at a radius less than 19 mm for the M-type and 14 mm for the S-type, 2.0 mm at radius between 14 and 20 mm for the S-type and between 19 and 25 mm for the M-type, and 3.0 mm in the outer area of the lug base (Figure 22). Static structural analysis for lugs with ribbing bushing requires additional mesh refining to a 0.25 mm size inside the radius of 9 mm from the lug axis, which led to an increase in the number of mesh elements to 34,302 for the S-type lug and 36,152 for the M-type lug.

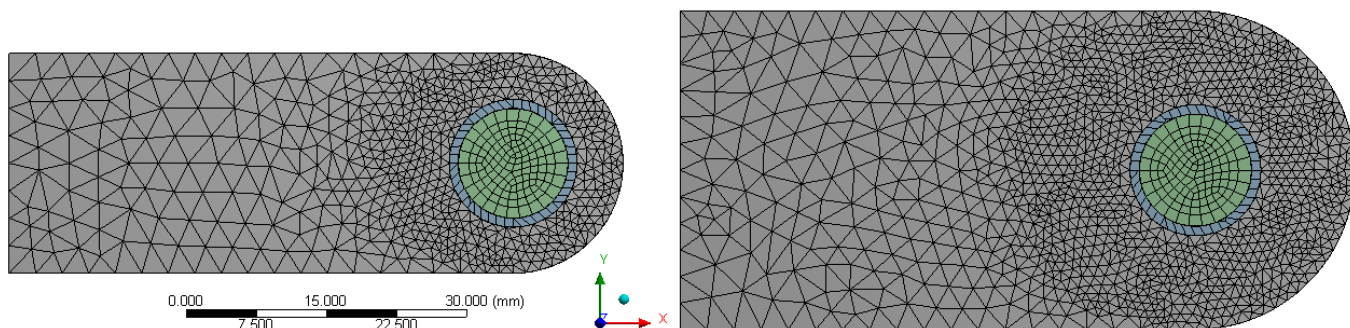


Figure 22. Computation mesh for tensile calculation of lugs for S-type and M-type lugs with ring-bushing. Grey is plastic part, blue is busing, green is axis.

The calculation is performed in a nonlinear formulation (Figure 23). The rear end of the lug is Fixed Supported. The loading is applied through displacement of the steel axis side surfaces along X by loading steps of (0.05, 0.1, 0.2, 0.3, 0.4 mm). The force on the lug axis is measured as the Force Reaction on this boundary condition. The lateral ribs of the lug and the bushing are additionally fixed by the condition $Z = 0$, to increase the computational stability of the problem. The chosen range of lug axis displacements ensures that the strength criterion and the loading on the lugs correspond to the breaking loading.

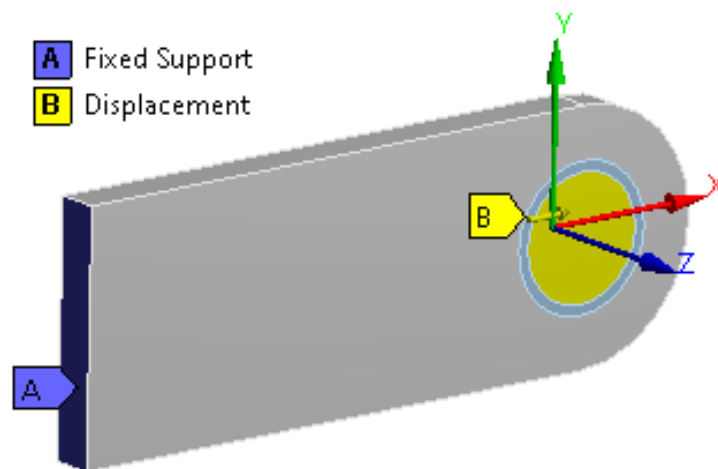


Figure 23. Boundary conditions for calculation. Grey is plastic part, dark blue is fixed support condition, light blue is bushing, yellow is displacement condition at axis.

The calculation was performed on one core of an Intel Core i7-5820K CPU @ 3.30 GHz for 600 s for the S-type lug and 1047 s for the M-type lug, a 103 MB maximum total memory was used, with a 2112 MB maximum total memory allocated. Convergence plots for the S-type and M-type lugs are shown at Figure 24.

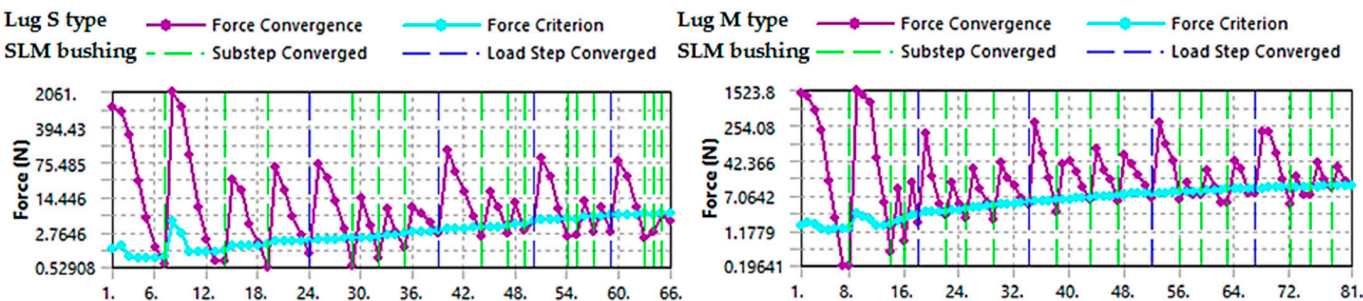


Figure 24. Convergence plots for S-type and M-type lugs with SLM bushing.

The lug load capacity (Table 4) is defined as the failure load at which the Tsai–Hill failure criterion (Figure 25) reaches 1 at least at one point of the lug. It may be noted that in the case of the study of ribbed bushing lugs using a fine mesh, this approach may be too strict, but we will stay with it so as not to bring in subjectivity. The time shown in Figure 25 corresponds to the loading step and can be used for results repeatability.

Table 4. Calculated lug load capacity with fitted CZM mode II parameters.

Surface	F max, N	
	S-Type	M-Type
Vibratory finishing	4741	6386
Sandblasting	6344	8052
SLM	7260	9220
Ribbing	7969	9160

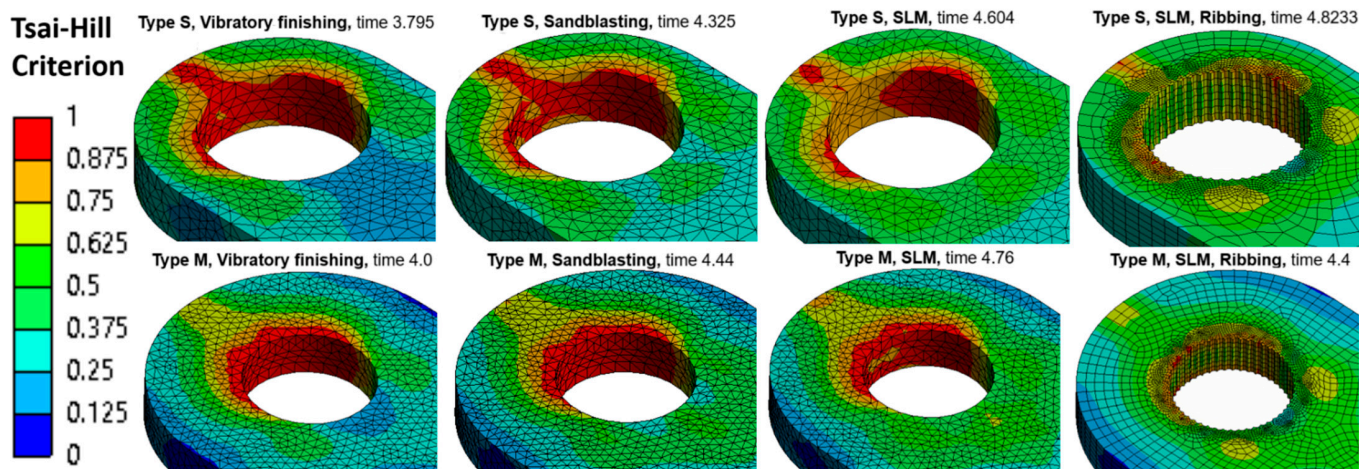


Figure 25. The Tsai–Hill failure criterion at the failure load moment.

Analysis of the figure shows that increasing the roughness of the sleeve leads to a more uniform stress field, which allows an increase in the failure load. Moreover, for S-type lugs, the area of the high values of the strength criterion in the front part of the lug near the weld line is reduced.

The experimental lugs' fracture happens in different ways (Figure 26): in the case of low roughness vibratory finishing bushings, the fracture is along the weld line (Figure 26a), whereas for lugs with SLM large roughness bushings, the side part is also destroyed (Figure 26b), which corresponds to the redistribution of the strength criterion field described above.

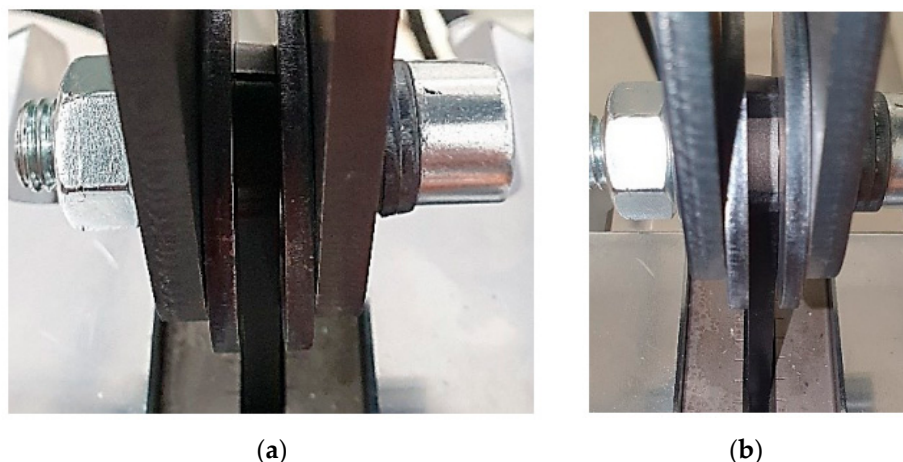


Figure 26. The lug fractures with different bushings: (a) vibratory finishing, (b) SLM bushing surface.

It is shown that the mathematical models used give a result that corresponds qualitatively—greater roughness gives greater load-bearing capacity and has load-bearing capacity values of the same order, but in the calculations, the influence of roughness on the load-bearing capacity is much stronger (see Table 4). In calculations, the difference between the load-bearing capacity of pin-joints with bushings with surface after SLM and vibratory finishing is 53% for the S-type and 44% for the M-type, whereas in experiments, this difference is 11% for the S-type and 3.5% for the M-type.

4. Discussion

It has been experimentally confirmed that an increase in the roughness of the embedded element leads to an increase in the load-bearing capacity of the lugs. Thus, compared with the surface obtained by vibratory finishing, the original surface after the SLM process gives a load-bearing capacity of the unit 11% higher for standard S-type and 3.5% higher for the standard M-type. For the S-type, during the design of which the contribution of the adhesive connection was considered, the influence of roughness is more noticeable than for the M-type, where the main load-bearing capacity lies on the lug body. The weight of the M-type lug is 17 g, which is 1.58 times more than the weight of the S-type lug (which weighs 10.7 g), and the maximum tensile load is only 1.42 times higher. Therefore, the S-type lug designed with an adhesive connection in mind has a weight efficiency that is 11.7% higher than that of the M-type lug. A comparison of the load-bearing capacity of lugs with a bushing and reference lugs without a bushing with the same internal and external diameters shows that the presence of a bushing with weak adhesion can lead to a decrease in the load-bearing capacity of the pin-joint compared with a pin-joint without an embedded element due to a reduction in the cross-sectional area of the plastic. The assumption about the importance of increasing the maximum equivalent tangential contact stress is confirmed by the fact that lugs with a bushing with ribs have a load-bearing capacity of 11% for the S-type and 8.6% for the M-type compared with lugs with a bushing of the same roughness, determined by the SLM process. Compared with lugs without bushings, the use of bushings with ribs increases the load-bearing capacity by 20% for the S-type and 11% for the M-type. The weight efficiency of an S-type lug with a bushing with ribs is 27% higher than that of an M-type lug without a bushing, which indicates the possibility of a significant reduction in weight with the development of SLM technology for the manufacture of embedded elements for aerospace designs. To determine the parameters of adhesive interaction in mode II, which determines damage caused by shear, extrusion tests were performed on bushings with varying degrees of roughness along the lug axis on a universal testing machine, Zwick/Roell Z050 TE. The forces acting on the bushing along the extrusion axis for surfaces provided by the SLM process, sandblasting, and vibratory

finishing are 2500, 1383, and 496 N, respectively. That is, sandblasting can reduce the plastic shear force by 45%, and vibrating finishing can reduce the contact shear force by 80%.

5. Conclusions

This article describes the results of a study on the load-bearing capacity of lugs with different surface roughness bushing. The CZM mode II of cohesive elements was used as the main model of contact interaction. The dimensions of the embedded elements are determined based on parametric optimization, taking into account the various types of contact interactions. An experimental study was conducted using an example of lugs of two sizes. More than 50 embedded bushings and more than 40 flat samples of three roughnesses provided by the initial SLM process, sandblasting, and vibratory finishing were manufactured using the SLM method. A tool and 35 injection molding parts were made, each of which contained lugs of two types and flat samples. Sixty lugs of two types and five types of bushings were tested, the surface of which was obtained by vibratory finishing, sandblasting, the SLM process, bushings with ribs, and lugs without a bushing. The rib height of the lug was 0.2 mm.

It has been shown that the use of sandblasting can reduce the shear force of plastic by 45%, and the use of vibratory finishing can reduce the shear force in contact by 80%. The mathematical models were refined based on the results of sample testing. A comparison was made of the strength of the designs with embedded elements made of short-reinforced composite materials obtained experimentally and by calculation. A comparison of the fields of the Tsai–Hill strength criterion with the places of destruction of the samples shows a correct prediction of the places of initiation of destruction.

The method used in this work to analyze the CZM mode II parameters can be successfully used when the fabrication of large standard crack opening samples is limited by the size of the equipment or by the materials' shrinkage. The advances in additive technologies, including their use for the production of topologically optimal embedded elements, may lead to an increase in using the contact pair between SFRP PA6 and SLM Ti-6Al-4V that will increase the practical significance of the parameters of their adhesive interaction determined in this work.

Author Contributions: Conceptualization, E.K. (Evgenii Kurkin); methodology, E.K. (Evgenii Kurkin), V.S. and S.C.; validation, E.K. (Evgenii Kurkin) and S.C.; formal analysis, E.K. (Evgenii Kishov), V.C. and V.A.; resources, A.S., V.S. and E.K. (Evgenii Kurkin); writing—original draft preparation, A.S., E.K. (Evgenii Kurkin) and V.C.; writing—review and editing, A.S., E.K. (Evgenii Kurkin), V.S., V.C., V.A., E.K. (Evgenii Kishov), A.G., M.Z. and S.C.; visualization, V.C., V.A., A.G. and M.Z.; supervision, E.K. (Evgenii Kurkin) and V.S.; project administration, E.K. (Evgenii Kurkin); funding acquisition, A.S. and E.K. (Evgenii Kurkin). All authors have read and agreed to the published version of the manuscript.

Funding: The study was financially supported by the Russian Science Foundation, project No. 22-79-10309.

Data Availability Statement: The data presented in this study are available on request from the corresponding author.

Acknowledgments: The authors thank G.V. Charkviani for helping with tool design and production. The authors thank Pladep Ltd. for their help in injection molding.

Conflicts of Interest: The authors declare no conflicts of interest. The funders had no role in the design of the study; in the collection, analyses, or interpretation of data; in the writing of the manuscript, or in the decision to publish the results.

References

1. Harris, C.E.; Starmes, J.H., Jr.; Shuart, M.J. Design and Manufacturing of Aerospace Composite Structures, State-of-the-Art Assessment. *J. Aircr.* **2002**, *39*, 545–560. [[CrossRef](#)]
2. Das, M.; Sahu, S.; Parhi, D.R. A Review of Application of Composite Materials for Aerospace Structures and its Damage Detection Using Artificial Intelligence Techniques. In Proceedings of the International Conference on Artificial Intelligence in Manufacturing & Renewable Energy (ICAIMRE), Bhubaneswar, India, 25–26 October 2019. 10p. [[CrossRef](#)]

3. Sriranga, B.K.; Kumar, R. Stress Analysis and Fatigue Life Prediction of Wing-Fuselage Lug Joint Attachment Bracket of a Transport Aircraft. *Int. J. Res. Eng. Technol.* **2014**, *3*, 818–822. [[CrossRef](#)]
4. Antoni, N.; Gaisne, F. Analytical Modelling for Static Stress Analysis of Pin-Loaded Lugs with Bush Fitting. *Appl. Math. Model.* **2011**, *35*, 1–21. [[CrossRef](#)]
5. Ekwall, J.C. Static Strength Analysis of Pin-Loaded Lugs. *J. Aircr.* **1986**, *23*, 438–443. [[CrossRef](#)]
6. Schijve, J.; Hoeymakers, A.H.W. Fatigue Crack Growth in Lugs and the Stress Intensity Factor. In *Delft University of Technology, Department of Aerospace Engineering, Report LR-273*; Delft University of Technology: Delft, The Netherlands, 1978.
7. Abraham, J. Pulickal Design Structural Analysis and Fatigue Calculation of Wing Fuselage Lug Attachment of a Transport Aircraft. *Int. J. Mag. Eng. Technol. Manag. Res.* **2017**, *4*, 60–65. Available online: <http://www.ijmetmr.com/olaugust2017/AbrahamJPulickal-DamodaraReddy-6.pdf> (accessed on 8 March 2024).
8. Sumanth, M.H.; Ayyappa, T. Comparative Analysis of Aircraft Wing Fuselage Lug Attachment Bracket. *Int. J. Technol. Res. Eng.* **2017**, *5*, 4422–4429.
9. Wallin, M.; Saarela, O.; Law, B.; Liehu, T. RTM Composite Lugs for High Load Transfer Applications. In Proceedings of the 25th Congress of the International Council of the Aeronautical Sciences, Hamburg, Germany, 3–8 September 2006; 9p. Available online: http://www.icas.org/ICAS_ARCHIVE/ICAS2006/PAPERS/448.PDF (accessed on 8 March 2024).
10. Kurkin, E.; Espinosa Barcenas, O.U.; Kishov, E.; Lukyanov, O. Topology Optimization and Efficiency Evaluation of Short-Fiber-Reinforced Composite Structures Considering Anisotropy. *Computation* **2024**, *12*, 35. [[CrossRef](#)]
11. Adin, H.; Bakir, G.S.; Özbay, M. Comparison of Different Bushing Applications in Composite Structures of the Aerospace Industry. *Mater. Test.* **2017**, *59*, 575–584. [[CrossRef](#)]
12. Kaya, N. Shape Optimization of Rubber Bushing Using Differential Evolution Algorithm. *Sci. World J.* **2014**, *379196*, 9. [[CrossRef](#)]
13. Bilal, H.; Ozturk, F. Rubber Bushing Optimization by Using a Novel Chaotic Krill Herd Optimization Algorithm. *Soft Comput.* **2021**, *25*, 14333–14355. [[CrossRef](#)]
14. Zhang, H.; Takezawa, A.; Ding, X.; Xu, S.; Duan, P.; Li, H.; Guo, H. Bi-material microstructural design of biodegradable composites using topology optimization. *Mater. Des.* **2021**, *209*, 109973. [[CrossRef](#)]
15. Fu, H.; Xu, H.; Liu, Y.; Yang, Z.; Kormakov, S.; Wu, D.; Sun, J. Overview of Injection Molding Technology for Processing Polymers and Their Composites. *ES Mater. Manuf.* **2020**, *8*, 3–23. [[CrossRef](#)]
16. Thompson, M.K.; Moroni, G.; Vaneker, T.; Fadel, G.; Campbell, R.; Gibson, I.; Bernard, A.; Schulz, J.; Graf, P.; Ahuja, B.; et al. Design for Additive Manufacturing: Trends, opportunities, considerations, and constraints. *CIRP Ann.* **2016**, *65*, 737–760. [[CrossRef](#)]
17. Awaja, F.; Gilbert, M.; Kelly, G.; Fox, B.; Pigram, P. Adhesion of Polymers. *Prog. Polym. Sci.* **2009**, *34*, 948–968. [[CrossRef](#)]
18. Titanium and Titanium Alloys. *Fundamentals and Applications*; Leyens, C., Peters, M., Eds.; WILEY-VCH Verlag GmbH & Co. KGaA: Weinheim, Germany, 2003.
19. Moiseyev, V.N. *Titanium Alloys: Russian Aircraft and Aerospace Application*; Fridlyander, J.N., Ed.; CRC Press: Boca Raton, FL, USA, 2005. [[CrossRef](#)]
20. Etesami, A.; Fotovvati, B.; Asadi, E. Heat Treatment of Ti-6Al-4V Alloy Manufactured by Laser-Based Powder-Bed Fusion: Process, Microstructures, and Mechanical Properties Correlations. *J. Alloys Compd.* **2022**, *895*, 162618. [[CrossRef](#)]
21. Kolesnikov, B.; Herbeck, L.; Fink, A. CFRP/titanium Hybrid Material for Improving Composite Bolted Joints. *Compos. Struct.* **2008**, *83*, 368–380. [[CrossRef](#)]
22. Agapovichev, A.; Sotov, A.; Kokareva, V.; Smelov, V.G.; Kyarimov, R. Study of the Structure and Mechanical Characteristics of Samples Obtained by Selective Laser Melting Technology from VT6 Alloy Metal Powder. *Nanosci. Technol. Int. J.* **2017**, *8*, 323–330. [[CrossRef](#)]
23. Aleksandrov, V.K.; Anoshkin, N.F.; Bochvar, G.A.; Brun, M.Y.; Gelman, A.A.; Dominin, I.I.; Djakonov, Y.A.; Elagina, L.A.; Ermanok, M.Z.; Zvereva, Z.F.; et al. *Semi-Finished Products from Titanium Alloys*; Metallurgiya Press: Moscow, Russia, 1979.
24. Heinz, A.; Haszler, A.; Keidel, C.; Moldenhauer, S.; Benedictus, R.; Miller, W.S. Recent Development in Aluminium Alloys for Aerospace Applications. *Mater. Sci. Eng.* **2000**, *280*, 102–107. [[CrossRef](#)]
25. Lugauer, F.P.; Kandler, A.; Meyer, S.P.; Wunderling, C.; Zaeh, M.F. Induction-Based Joining of Titanium with Thermoplastics. *Prod. Eng. Res. Devel.* **2019**, *13*, 409–424. [[CrossRef](#)]
26. Du, K.; Huang, J.; Li, C.; Chen, J.; Li, Y.; Yang, C.; Xia, X.; Sheng, X. The Bonding Strength of Polyamide-6 Direct Adhesion with Anodized AA5754 Aluminum Alloy. *J. Thermoplast. Compos. Mater.* **2020**, *35*, 1852–1865. [[CrossRef](#)]
27. Reisgen, U.; Schleser, M.; Scheik, S.; Michaeli, W.; Grönlund, O.; Neuß, A.; Jakob, M. Novel Process Chains for the Production of Plastics/Metal-Hybrids. In Proceedings of the 17th International Conference on Concurrent Enterprising (ICE 2011), Aachen, Germany, 20–22 June 2011.
28. Ehrig, F.; Wey, H.-R. In-Mold Decoration: Foil Technology for Metal Surfaces. *Kunststoffe Int.* **2007**, *97*, 38–40.
29. Molitor, P.; Barron, V.; Young, T. Surface Treatment of Titanium for Adhesive Bonding to Polymer Composites: A Review. *Int. J. Adhes. Adhes.* **2001**, *21*, 129–136. [[CrossRef](#)]
30. Schricker, K.; Schmitt, L.; Grätzel, M.; Ecke, G.; Bergmann, J. Bonding Mechanisms in Laser-Assisted Joining of Metal-Polymer Composites. *J. Adv. Join. Process.* **2020**, *1*, 100008. [[CrossRef](#)]
31. Li, M.; Xiong, X.; Ji, S.; Hu, W.; Yue, Y. Achieving High-Quality Metal to Polymer-Matrix Composites Joint via Topthe Mic Solid-State Lap Joining. *Compos. Part B Eng.* **2021**, *219*, 108941. [[CrossRef](#)]

32. Jun, G.; Lee, J.-W.; Shin, Y.; Kim, K.; Hwang, W. Solvent-Aided Direct Adhesion of a Metal/Polymer Joint using Micro/Nano Hierarchical Structures. *J. Mater. Process. Technol.* **2020**, *285*, 116744. [[CrossRef](#)]
33. Ding, Z.; Wang, H.; Luo, J.; Li, N. A Review on Forming Technologies of Fibre Metal Laminates. *Int. J. Lightweight Mater. Manuf.* **2020**, *4*, 110–126. [[CrossRef](#)]
34. Critchlow, G.W.; Brewis, D.M. Review of Surface Pretreatments for Titanium Alloys. *Int. J. Adhes. Adhes.* **1995**, *15*, 161–172. [[CrossRef](#)]
35. Chanthapan, S.; Wattanapornphan, P.; Phongphisutthinan, C.; Kawahito, Y.; Suga, T. Effects of Oxide Layer on Adhesion and Durability of Titanium and Transparent Polyamide Joint by Laser Joining. *J. Laser Appl.* **2018**, *30*, 042005. [[CrossRef](#)]
36. Roesner, A.; Scheik, S.; Olowinsky, A.; Gillner, A.; Reisgen, U.; Schleser, M. Laser Assisted Joining of Plastic Metal Hybrids. *Phys. Procedia* **2011**, *37*, 370–377. [[CrossRef](#)]
37. Heckert, A.; Zaeh, M.F. Laser Surface Pre-Treatment of Aluminium for Hybrid Joints with Glass Fibre Reinforced Thermoplastics. *Phys. Proc.* **2014**, *56*, 1171–1181. [[CrossRef](#)]
38. Wang, Z.; Bi, X.; Liu, B.; Xu, M.; Dong, Z. Adhesion Enhancement of PEEK/6161-T6 FLJ Joints via Laser Surface Modification. *Compos. Part B Eng.* **2021**, *216*, 108797. [[CrossRef](#)]
39. Vasconcelos, R.; Marcatto de Oliveira, G.; Amancio-Filho, S.; Bresciani Canto, L. Injection Overmolding of Polymer-Metal Hybrid Structures: A Review. *Polym. Eng. Sci.* **2023**, *63*, 691–722. [[CrossRef](#)]
40. Kinloch, A.J. *Durability of Structural Adhesives*; Elsevier Applied Science: Barking, UK, 1983; pp. 15–16.
41. Du, M.; Dong, W.; Li, X.; Wang, L.; Wang, B.; Tang, B. Effect of Surface Topography on Injection Joining Ti Alloy for Improved Bonding Strength of Metal-Polymer. *Surf. Coat. Technol.* **2022**, *433*, 128132. [[CrossRef](#)]
42. Larimian, T.; Borkar, T. Additive Manufacturing of In Situ Metal Matrix Composites. In *Additive Manufacturing of Emerging Materials*; Springer International Publishing: Cham, Switzerland, 2018. [[CrossRef](#)]
43. Wang, Z.; Xie, M.; Li, Y.; Zhang, W.; Yang, C.; Kollo, L.; Eckert, J.; Prashanth, K.G. Premature Failure of an Additively Manufactured Material. *NPG Asia Mater.* **2020**, *12*, 30. [[CrossRef](#)]
44. Singh, N.; Ummethala, R.; Hameed, P.; Sokkalingam, R.; Prashanth, K.G. Competition Between Densification and Microstructure of Functional Materials by Selective Laser Melting. *Mater. Des. Process. Commun.* **2020**, *2*, e146. [[CrossRef](#)]
45. Prashanth, K.G.; Scudino, S. Quasicrystalline Composites by Additive Manufacturing. *Key Eng. Mater.* **2019**, *818*, 72–76. [[CrossRef](#)]
46. Singh, N.; Hameed, P.; Ummethala, R.; Manivasagam, G.; Prashanth, K.G.; Eckert, J. Selective Laser Manufacturing of Ti-Based Alloys and Composites: Impact of Process Parameters, Application Trends, and Future Prospects. *Mater. Today Adv.* **2020**, *8*, 100097. [[CrossRef](#)]
47. Abrate, S.; Ferrero, J.-F.; Navarro, P. Cohesive Zone Models and Impact Damage Predictions for Composite Structures. *Meccanica* **2015**, *50*, 2587–2620. [[CrossRef](#)]
48. Pegorin, F.; Pingkarawat, K.; Mouritz, A.P. Comparative Study of the Mode I and Mode II Delamination Fatigue Properties of Z-Pinned Aircraft Composites. *Mater. Des.* **2015**, *65*, 139–146. [[CrossRef](#)]
49. Asp, L.E.; Sjögren, A.; Greenhalgh, E.S. Delamination Growth and Thresholds in a Carbon/Epoxy Composite under Fatigue Loading. *Compos. Technol. Res.* **2001**, *23*, 55–68. [[CrossRef](#)]
50. Hojo, M.; Ando, T.; Tanaka, M.; Adachi, T.; Ochiai, S.; Endo, Y. Modes I and II Interlaminar Fracture Toughness and Fatigue Delamination of CF/Epoxy Laminates with Self-Same Epoxy Interleaf. *Int. J. Fatigue* **2006**, *28*, 1154–1165. [[CrossRef](#)]
51. Argüelles, A.; Vina, J.; Canteli, A.F.; Castrillo, M.A.; Bonhomme, J. Interlaminar Crack Initiation and Growth Rate in a Carbon-Fibre Epoxy Composite under Mode-I Fatigue Loading. *Compos. Sci. Technol.* **2008**, *68*, 2325–2331. [[CrossRef](#)]
52. Thouless, M.; Parmigiani, J. Mixed-Mode Cohesive-Zone Models for Delamination and Deflection in Composites. In Proceedings of the 28th Risø International Symposium on Material Science: Interface Design of Polymer matrix Composites, Roskilde, Denmark, 3–6 September 2007.
53. Evans, A.G.; Hutchinson, J.W. Effects of Non-Planarity on the Mixed Mode Fracture Resistance of Bimaterial Interfaces. *Acta Metall.* **1989**, *37*, 909–916. [[CrossRef](#)]
54. Cao, H.C.; Thouless, M.D.; Evans, A.G. Residual Stresses and Cracking in Brittle Solids Bonded with a Thin Ductile Layer. *Acta Metall.* **1988**, *36*, 2037–2046. [[CrossRef](#)]
55. Kurkin, E.; Kishov, E.; Chertykovtseva, V. Influence of Cohesive Zone Model Parameters of Polymer Lugs with Metal Bushing on Their Geometrical and Mass Characteristics. *Aerosp. Syst.* **2023**, *7*, 103–111. [[CrossRef](#)]
56. Reis, J.P.; de Moura, M.F.S.F.; Moreira, R.D.F.; Silva, F.G.A. Pure Mode I and II Interlaminar Fracture Characterization of Carbon-Fibre Reinforced Polyamide Composite. *Compos. Part B Eng.* **2019**, *169*, 126–132. [[CrossRef](#)]
57. Li, X.; Wang, B.; Xu, D.; Wang, B.; Dong, W.; Li, M. Super-High Bonding Strength of Polyphenylene Sulfide-Aluminum Alloy Composite Structure Achieved by Facile Molding Methods. *Compos. Part B Eng.* **2021**, *224*, 109204. [[CrossRef](#)]
58. Mahaphasukwat, S.; Shimamoto, K.; Hayashida, S.; Sekiguchi, Y.; Sato, C. Mode I Critical Fracture Energy of Adhesively Bonded Joints between Glass Fiber Reinforced Thermoplastics. *Appl. Adhes. Sci.* **2015**, *3*, 4. [[CrossRef](#)]
59. Duda, S.; Smolnicki, M.; Osiecki, T.; Lesiuk, G. Determination of Fracture Energy (Mode I) in the Inverse Fiber Metal Laminates using Experimental–Numerical Approach. *Int. J. Fract.* **2022**, *234*, 213–222. [[CrossRef](#)]
60. Matinmanesh, A.; Li, Y.; Clarkin, O.; Zalzal, P.; Schemitsch, E.H.; Towler, M.R.; Papini, M. Quantifying the Mode II Critical Strain Energy Release Rate of Borate Bioactive Glass Coatings on Ti6Al4V Substrates. *J. Mech. Behav. Biomed. Mater.* **2017**, *75*, 212–221. [[CrossRef](#)]

61. Tsokanas, P.; Loutas, T.; Nijhuis, P. Interfacial Fracture Toughness Assessment of a New Titanium–CFRP Adhesive Joint: An Experimental Comparative Study. *Metals* **2020**, *10*, 699. [[CrossRef](#)]
62. Kurkin, E.I.; Spirina, M.O.; Espinosa Barcenas, O.U.; Kurkina, E.V. Calibration of the PA6 Short-Fiber Reinforced Material Model for 10% to 30% Carbon Mass Fraction Mechanical Characteristic Prediction. *Polymers* **2022**, *14*, 1781. [[CrossRef](#)] [[PubMed](#)]
63. ISO-527-2-2012; Plastics. Determination of Tensile Properties. International Standard: Geneva, Switzerland. Available online: <https://www.iso.org/standard/56046.html> (accessed on 8 March 2024).
64. Gamma-Plast UPA 6 30 M. Available online: <https://gamma-plast.ru/poliamid/uglenapolnenniy/poliamid-upa-6-30-m/> (accessed on 8 March 2024).
65. ZwickRoell LP. Available online: <https://www.zwickroell.com/ru/produkcia/staticheskie-ispytatelnye-mashiny/universalnye-mashiny-dlya-staticheskikh-ispytanii/allroundline/> (accessed on 8 March 2024).
66. Alfano, G.; Crisfield, M.A. Finite element interface models for the delamination analysis of laminated composites: Mechanical and computational issues. *Int. J. Numer. Methods Eng.* **2001**, *50*, 1701–1736. [[CrossRef](#)]
67. ASTM D7905/D7905M-19e1; Standard Test Method for Determination of the Mode II Interlaminar Fracture Toughness of Unidirectional Fiber-Reinforced Polymer Matrix Composites. ASTM International: West Conshohocken, PA, USA, 2019. [[CrossRef](#)]
68. GOST 4784-97; Aluminium and Wrought Aluminium Alloys. Grades, Standartinform: Moscow, Russia, 2009.
69. Aluminum 2024-T4; 2024-T351. Available online: https://www.matweb.com/search/datasheet_print.aspx?matguid=67d8cd7c00a04ba29b618484f7ff7524 (accessed on 2 May 2024).
70. SHIMADZU. Available online: <https://www.shimadzu.com/an/products/materials-testing/fatigue-testing/impact-testing/ehf-e-series/index.html> (accessed on 8 March 2024).
71. Negri Bossi: Global Injection Moulding Machine Supplier. Available online: <https://www.negribossi.com/> (accessed on 8 March 2024).
72. Akromid B3 ICF 30 Black. Available online: <https://akro-plastic.com/en/product/akromid-b3-icf-30-schwarz-5119-de> (accessed on 8 March 2024).
73. Cross, M.M. Rheology of non-Newtonian fluids: A New flow equation for pseudo-plastic systems. *J. Colloid Sci.* **1965**, *20*, 417–437. [[CrossRef](#)]
74. Digimat, M.F. User’s Guide. Available online: https://help-be.hexagonmi.com/bundle/Digimat_2023.1_MF_User_Guide/raw/resource/enus/Digimat_2023.1_MF_User_Guide.pdf (accessed on 2 May 2024).
75. Van Hattum, F.W.J.; Bernardo, C.A. A model to predict the strength of short fiber composites. *Polym. Compos.* **1999**, *20*, 524–533. [[CrossRef](#)]

Disclaimer/Publisher’s Note: The statements, opinions and data contained in all publications are solely those of the individual author(s) and contributor(s) and not of MDPI and/or the editor(s). MDPI and/or the editor(s) disclaim responsibility for any injury to people or property resulting from any ideas, methods, instructions or products referred to in the content.